Droplet formation and scaling in dense suspensions

Marc Z. Miskin and Heinrich M. Jaeger[1]

James Franck Institute, University of Chicago, 929 East 57th Street, Chicago, IL 60637

Edited by Jerry P. Gollub, Haverford College, Haverford, PA, and approved January 20, 2012 (received for review July 8, 2011)

When a dense suspension is squeezed from a nozzle, droplet detachment can occur similar to that of pure liquids. While in pure liquids the process of droplet detachment is well characterized through self-similar profiles and known scaling laws, we show here the simple presence of particles causes suspensions to break up in a new fashion. Using high-speed imaging, we find that detachment of a suspension drop is described by a power law; specifically we find the neck minimum radius, r_m, scales like $\tau^{\frac{2}{3}}$ near breakup at time $\tau = 0$. We demonstrate data collapse in a variety of particle/liquid combinations, packing fractions, solvent viscosities, and initial conditions. We argue that this scaling is a consequence of particles deforming the neck surface, thereby creating a pressure that is balanced by inertia, and show how it emerges from topological constraints that relate particle configurations with macroscopic Gaussian curvature. This new type of scaling, uniquely enforced by geometry and regulated by the particles, displays memory of its initial conditions, fails to be self-similar, and has implications for the pressure given at generic suspension interfaces.

particle packing | contact angle | irrotational flow | jamming

The rupture of a single volume filled with matter to produce two unconnected volumes, a transition between two distinct topologies, plays a fundamental role in a wide range of phenomena from dripping liquids (1, 2), to breakup of nano-jets (3–5), to metal rods pinching off (6), to black-string instabilities in general relativity (7, 8). In biological systems, topological transitions are equally fundamental because they govern processes like cell division (9), endocytosis (10), and collapsing bacterial colonies (11).

Of these examples, liquid droplet formation is particularly notable because it exhibits many of the exotic features of a topological transition, such as singularities and scaling, while being accessible enough to warrant thorough experimental examination (12–18). The result has been a powerful framework that characterizes the final moments of pure liquid droplet detachments using only the relative strengths of surface tension, viscous dissipation, and inertial stress (1, 2). For these liquids, the initial conditions become irrelevant as the system nears the singular point of snap off. Instead, the material parameters alone assign both a self-similar profile defining the shape of the drop and a power law governing how this shape scales close to the final moments of breaking.

The success of self-similarity and scaling approaches has prompted attempts to extend pure liquid analysis to other instances of free surface flows. In many cases, when the boundary stresses originate from surface tension, the framework of pure liquid detachment can be modified successfully and self-similar structures govern the breakup (19–21). However, in some cases the driving force comes from an alternative source, as in the case of bubble pinch-off (22–24), and self-similarity breaks down: To describe detachment, scaling laws must be used along with initial conditions.

For suspensions, the boundary stresses can be notoriously complex: The presence of particles within the liquid admits the possibility of protrusions that establish a local stress scale independent of the global mean curvature (25, 26). Although previous work (27–30) has sought to connect pure liquids with suspensions, these deformations leave it unclear as to whether the framework of pure liquid breakup, specifically self-similarity and scaling, can be used, or if suspension breakup represents a new class of topological transition outside the canon of pure liquids. We find strong experimental evidence for the latter: The presence of particle protrusions cannot be ignored, or even treated as a small perturbation, but instead necessitates an entirely new description of the boundary stress and by extension a new type of topological transition.

Results and Discussion

When a highly concentrated suspension is slowly extruded through a nozzle, it will squeeze out as a plug and then begin to strain near the nozzle from gravitational stress. Eventually this stress becomes too large and the sample starts to yield. Upon failure, the suspension profile will begin to thin down to detach (Fig. 1*A*). Throughout this necking process, a dense suspension will maintain a vertically symmetric bridge profile with a steadily decreasing minimum neck radius. Ultimately, the thinning leaves just two particles connected by a small, vertical bridge of liquid. At this point, the particle size acts as an intrinsic cutoff scale for suspension thinning, because the rupture of the liquid thread between the two final particles proceeds within the solvent only. Our study focuses on the regime prior to this final necking for suspensions of packing fractions larger than 50%, where we show how the breakup is driven by the interplay of particles, liquid, and initial conditions.

Comparing the profile shape of a dense suspension (Fig. 1*C*) to that of a pure liquid (Fig. 1*D*), the symmetry about the minimum of the average neck profile in a suspension stands in stark contrast to the asymmetric profile of the pure liquid in its final stages. Early in detachment, high viscosity liquids can exhibit symmetric profiles (1, 2), and consequently previous authors (29) have attempted to connect the observed rate of thinning for the neck with self-similar scaling predictions for high viscosity liquids. However, while an interpretation of dense suspensions as simply very viscous fluids is appealing from a rheological point of view (31), quantitative description of detachment eliminates this perspective: As shown in Fig. 2, the neck minimum radius near breakup, r_m, decreases with time to breakup, τ, slower than the linear scaling, $r_m \sim \tau$, predicted near detachment for the high viscosity limit (1, 2). Instead, $r_m(\tau)$ follows a power law $r_m \sim \tau^{\frac{2}{3}}$ over almost two and a half decades of time (Fig. 2).

The presence of a 2/3 scaling exponent can imply a variety of different physics. For instance, a 2/3 exponent results from the force balance between inertia and surface tension, which governs the pinch-off of inviscid liquids like water (18). Yet the simple fact that dense suspensions can have shear viscosities on the order of 1 Pa s (32, 33) makes a connection to inviscid pinch-off counterintuitive. Further, barring an initial transient regime, the bridge profile for inviscid pinch-off is markedly asymmetric (18). Other systems displaying a 2/3 exponent that are always symmetric include clustering granular jets (34, 35) and pinching power-law

Author contributions: M.Z.M. and H.M.J. designed research; M.Z.M. performed research; M.Z.M. analyzed data; and M.Z.M. and H.M.J. wrote the paper.

The authors declare no conflict of interest.

This article is a PNAS Direct Submission.

[1]To whom correspondence should be addressed. E-mail: h-jaeger@uchicago.edu.

This article contains supporting information online at www.pnas.org/lookup/suppl/doi:10.1073/pnas.1111060109/-/DCSupplemental.

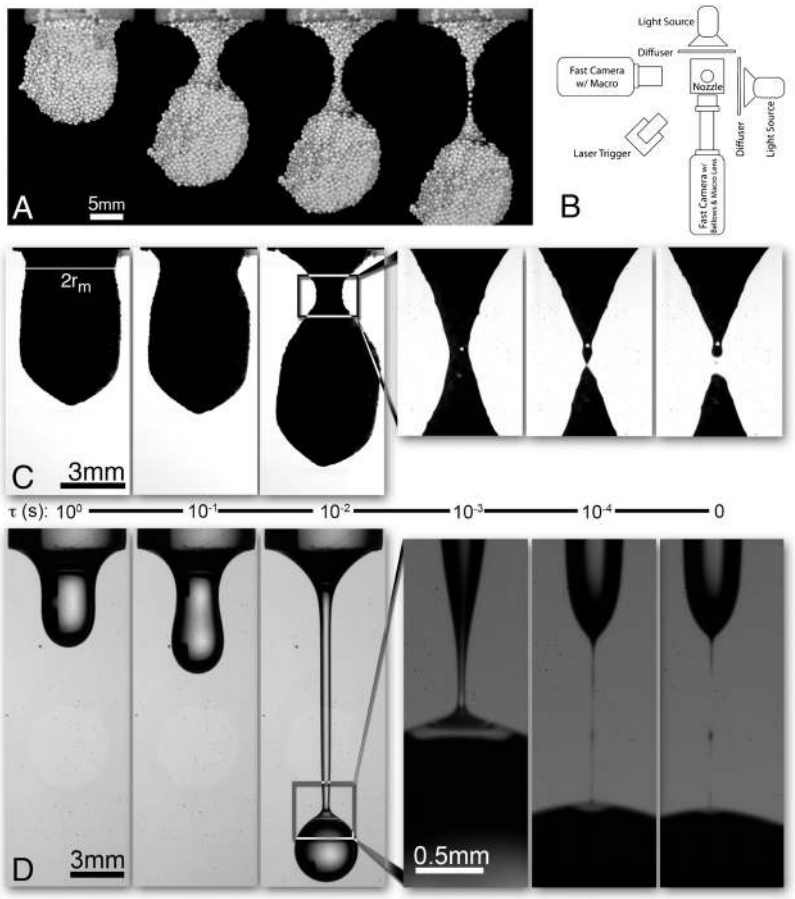

Fig. 1. Contrasting droplet formation in dense suspensions and pure liquids. (*A*) Images of a suspension droplet made from 850 μm zirconium dioxide suspended in water ($\phi = 0.63$ +0.01/-0.02) detaching from a 14.5-mm diameter nozzle. The symmetric profile maintains itself until the neck is only one particle thick, and the small liquid bridge adjoining particles ruptures. (*B*) Schematic of our experimental configuration, which uses two cameras to achieve a spatial resolution of 4.4 μm and a temporal resolution of $10^{-4}s$. (*C* and *D*) Comparison of 145 μm zirconium dioxide suspended in water ($\phi = 0.59 \pm 0.02$) (*C*) and pure 50 cst silicone oil (*D*), both exiting a 4.7-mm diameter nozzle. Each panel is an order of magnitude closer to breakup at time $\tau = 0$. Note the asymmetry and increased elongation exhibited by the pure fluid. See Movies S1–S3.

fluids (20, 21), though in these cases the thinning mechanism is related to types of dissipation. To discern which, if any, of these systems are similar to dense suspension pinch-off, we systematically changed material properties and initial conditions searching for indicative variation in the thinning power law.

Varying these experimental conditions can delay the onset of this scaling but not eliminate it: Early time behavior of $r_m(\tau)$ can be material dependent (Fig. 3*A*) and/or vary with initial conditions, such as changes in nozzle size (Fig. 3*B*). When the packing fraction is reduced we find that the early stages of detachment mimic the behavior of a pure liquid of matched effective viscosity (Fig. 3*C*), in agreement with previous work (27, 29). Yet it should be noted that this regime, being far from breakup, depends strongly on initial conditions, and therefore even the pure liquid cannot be described by simple scaling arguments. Instead, where scaling arguments do describe the viscous liquid, it thins as τ^1, while the suspension thins according to $\tau^{\frac{2}{3}}$. Independence of neck thinning from packing fraction and compatibility with 2/3 scaling has been suggested by authors working in the more dilute limit (29). Further the presence of this exponent, even at such low packing fractions, implies that for much denser suspensions, the packing fraction is an inessential parameter in describing scaling. The data in Fig. 3 show that, close to breakup, the 2/3 scaling exponent is even more robust and applies deep into the regime of dense suspensions, independent of particle composition or diameter, and nozzle diameter.

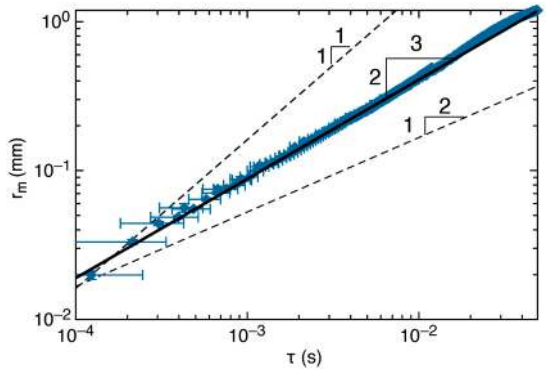

Fig. 2. Evolution of the minimum neck radius, r_m, as a function of time to breakup, τ, for 22-μm diameter glass particles in water ($\phi = 0.61 \pm 0.02$) exiting a 4.7-mm diameter nozzle. In this type of plot, time increases from right to left. A neck width corresponding to a single particle radius, the natural cutoff of the breakup process discussed here, is reached at the left edge of the plot. Different power laws are indicated for comparison: τ is the power law for viscous breakup (1, 2), $\tau^{\frac{1}{2}}$ is the power law for bubble pinch-off (23), and $\tau^{\frac{2}{3}}$ is the power law predicted by Eq. **2**.

Examining the dependence of the prefactor of the power law shows further disagreement with any models relating the scaling behavior to viscous stress. Fig. 3*A* shows that altering the solvent viscosity by two orders of magnitude has little to no effect on the scaling near breakup, while decreasing the surface tension by only threefold reduces the prefactor of the power law noticeably. The independence of both exponent and prefactor from the solvent viscosity over the range investigated implies that, near breakup, viscous dissipation is inconsequential.

On the other hand, the finite particle size clearly has to come into play as the suspension neck thins down. In the images in Fig. 1 we see that the bounding surface is littered with deformations from protruding particles, and Fig. 3*D* clearly shows a dependence of the power-law prefactor on particle size. In fact, even at much lower packing fractions, particle-induced deformations

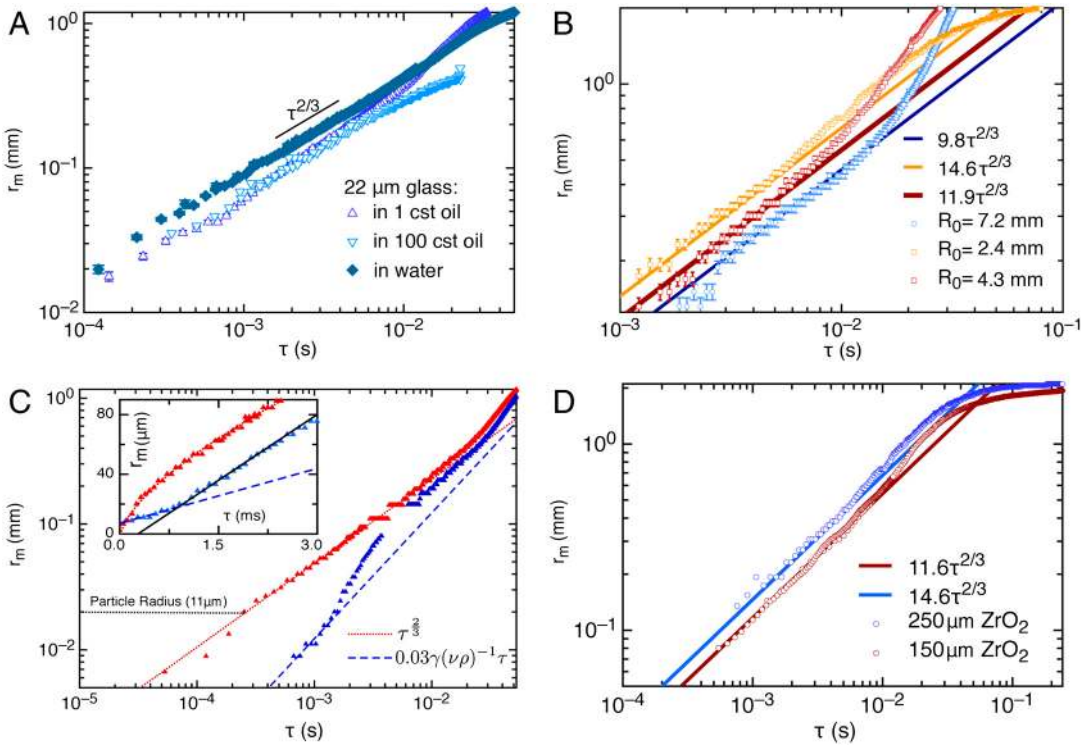

Fig. 3. Representative data for different solvents (*A*), nozzle radii (*B*), particle diameters (*D*), and a direct comparison of a suspension and a pure liquid with the same effective viscosity (*C*). Comparing 22-μm glass suspended in water with 1 cst silicone oil and 100 cst silicone oil, all exiting the 2.4-mm radius nozzle, data for two systems with comparable surface tension are more similar than data for systems with the same viscosity (*A*). Varying the nozzle radius between 2.4 mm, 4.3 mm, and 7.2 mm for 250 μm ZrO_2 suspended in water yields prefactors $\sim 25/R_0^{\frac{1}{3}}$, which similarly agree with Eq. **2** (*B*). Data for 150 μm and 250 μm ZrO_2 exiting a 2.4-mm radius nozzle shows that the ratio of the prefactors, 0.8, is within 5% of $(150/250)^{\frac{1}{3}}$, the ratio predicted by Eq. **2** (*D*). Comparison of 33-μm polyethylene particles at packing fraction of 25% in a density matched oil with a pure silicone oil of the same effective viscosity (50 cst) (*C*). Early in the breakup there is strong similarity between the suspension and the pure liquid, but near detachment the two curves diverge. In particular, as shown in the inset, the pure liquid thins linearly with time, first in the Stokes then in the Eggers regime (1, 2). As a result, the ratio of the linear slopes in the inset is 2.4, as predicted. The suspension, on the other hand, thins nonlinearly, decaying like $\tau^{\frac{2}{3}}$.

dominate the local curvature in the neck region (28). Therefore, the local pressure at the surface may not be related to the macroscopic mean curvature, as in the Laplace–Young equation, but instead to particle-induced menisci.

Altogether these results suggest that available approaches (1, 2, 21, 30) based on liquid models cannot adequately describe suspension behavior near breakup (*SI Text*). They also call into question recent attempts to characterize thinning near breakup by scaling expressions derived for very viscous liquids (29). Instead, a new, more tailored description must be constructed that pays attention to the microscopic deformations from particles and at the same time acknowledges the experimental evidence that viscous stresses are negligible.

To develop such a description, we start with the force exerted by the liquid on a particle protruding through the surface of the suspension. This force scales as $F_p = \alpha\gamma a$ where γ is the surface tension, a the particle diameter, and α a constant of order unity related to the contact angle and the depth of immersion (26). The pressure on the surface from n of these particles contained within some characteristic area A is then $P = \alpha\gamma a/S_{pp}$, where S_{pp} is the surface area per particle, $\frac{A}{n}$. This expression relates the pressure to the particle configuration on the surface. If the surface were flat, S_{pp} would be, on average, a constant. However, on a surface that is curved inward like the neck region, the physics are richer: Surfaces with Gaussian curvature can accommodate variations in packing (36–39) and therefore the curvature mediates a feedback between particle packing and pressure.

The packing structure can be related directly to the Gaussian curvature K by considering a geodesic triangulation among n particles. Using the Gauss–Bonnet and Euler–Poincaré theorems and ignoring edge effects, the integral over the area is $\int K dA = \frac{\pi}{3}(6 - \bar{Z})n$, where $\bar{Z}$ is the mean coordination number in the triangulation (37, 40). We now note that near the neck minimum radius, the curvature is roughly constant. This allows us to make the approximation $K/(\frac{\pi}{3}(6 - \bar{Z})) = \frac{n}{A}$. Identifying the right hand side of this equation as S_{pp} and combining it with the pressure expression gives $P = \alpha\gamma a K/\frac{\pi}{3}(6 - \bar{Z})$.

Simulations of locally disordered packings on curved 2D spaces reveal that $\bar{Z}$ is set by the number of spheres that can be brought in contact around a given sphere on the surface (*SI Text*). That is, $\bar{Z} \approx 2\pi/\arccos\left(\frac{\cosh(2\sqrt{-Ka})}{1+\cosh(2\sqrt{-Ka})}\right)$ (38, 39). Because both principle radii are always larger than the particle size, the pressure expression can be expanded around $\sqrt{-K}a = 0$. This leads to

$$P = -\alpha\gamma\left[\frac{1}{2\sqrt{3}a} + \frac{(6-\sqrt{3}\pi)}{12\pi}Ka + \mathcal{O}(\sqrt{-Ka})^3\right]. \quad [1]$$

The first term in Eq. **1** represents the constant capillary stress that would result from hexagonal close packing on a flat surface. This term, while a crucial component in describing shear thickening in dense suspensions (32, 33), is constant everywhere and therefore does not contribute to the gradient needed to create flow. The second term, however, varies along the surface and can drive the flow causing breakup. This result, together with conservation of momentum, can now be used to create a scaling argument.

The close packing of the grains will lead to stresses that are constant along the radial direction but vary along the axial scale due to differences in the confining pressure. This has

two repercussions: First, it implies that the dominant flow should be in the z direction. Second, it produces a flow that is largely irrotational, removing viscous stress from the flow equations, as observed in the experiments.

Balancing the remaining stress from the gradient of the pressure and the inertial force density gives (*SI Text*) $\rho\frac{r_m}{\tau^2}\sim\frac{\Lambda\gamma a K|_{r_m}}{r_m}$, where $K|_{r_m}$ is the Gaussian curvature at the neck minimum, and for simplicity we absorb all the numerical prefactors and α into a new constant $\Lambda\propto\alpha$. Volume conservation, jamming, and symmetry arguments can be used to show that the axial principal radius near the minimum must converge to the initial nozzle radius, R_0 (*SI Text*). Therefore, $K|_{r_m}=-1/(r_m R_0)$. This lets us write our scaling expression as

$$r_m\sim\left(\frac{\Lambda\gamma a}{\rho R_0}\right)^{\frac{1}{3}}\tau^{\frac{2}{3}}. \qquad [2]$$

Dividing both sides of Eq. **2** by the initial nozzle radius, we obtain the nondimensional variables characterizing the intrinsic length and time scales for the breakup process,

$$\bar{R}=r_m/R_0,\quad \bar{\tau}=\tau/\left[\frac{\rho R_0^4}{\Lambda\gamma a}\right]^{\frac{1}{2}}. \qquad [3]$$

As shown in Fig. 4, applying this scaling collapses data for a wide range of different particle types and sizes, and agrees to within a prefactor of $\mathcal{O}(1)$.

Fig. 4 demonstrates that the remaining variation can be related to the particle-solvent chemistry. Glass, the material most easily wet by water, has the largest prefactor, polystyrene, which is the most hydrophobic material, has the smallest prefactor, and zirconium dioxide, which is mildly hydrophobic, exhibits an intermediate value. This dependence is fully consistent with our model because a more realistic representation of the force $F_p=\alpha\gamma a$ on a particle from the liquid treats α not as a constant but includes an explicit dependence on the solid-air contact angle, θ, and the immersion angle, ϕ, measured from the top of the protruding sphere to the contact point with the liquid (26). Explicitly, $\alpha=\sin(\phi)\sin(\theta+\phi)$. To show this quantitatively, we vertically shift representative data from Fig. 4*A* onto a single curve (Fig. 4*B*) and plot the values for Λ required for this collapse as a function of measured solid-air contact angle θ (Fig. 4*B*, *Inset*). Because $\Lambda\propto\alpha$, better wetting, and thus larger solid-air contact angle θ, increases Λ and thus the prefactor in Eq. **2**. Moreover, a fit to $\Lambda(\theta)$ allows us to extract estimates for the immersion angle and the numerical constant, resulting in $\phi\sim 50^\circ$ and $\Lambda\approx 3\alpha$.

Inspection of Eqs. **2** and **3** allows us to establish a connection with the breakup scaling in inviscid liquids (18), where early in detachment the same 2/3 exponent is observed and the nondimensionalized variables are $\bar{R}=R_m/R_0$, and $\bar{\tau}=\tau/[\frac{\rho R_0^3}{\gamma}]^{\frac{1}{2}}$. Such $\bar{\tau}$ is reproduced by Eq. **2** when $R_0/a=1$. This predicts a suspension to behave like an inviscid liquid in the limit that the particle diameter approaches the scale of the nozzle. In other words, behavior similar to a molecular liquid is recovered not for vanishing particle diameter but once the particles become clearly visible to the naked eye!

Though at first glance paradoxical, the validity of this argument emerges when the role of surface tension is considered. For a pure liquid, the characteristic length for surface tension is related to the curvature induced by the droplet hanging from the nozzle. For the suspension, surface tension creates pressure from small particle menisci. If the mean curvature from each meniscus becomes comparable to the mean curvature from the sagging pendant drop, these two pressure scales converge. Fig. 5*A* shows that this is indeed what happens: As the particle size approaches the nozzle diameter, in this case 0.7 mm diameter zirconium dioxide particles in a 4.7 mm nozzle, the scaling of the neck minimum conforms to that of a pure inviscid liquid.

The analogy can be pushed even further and tested on the axial evolution of the neck. During the early stages of inviscid liquid pinch-off the axial curvature scale stays constant (18). Therefore, if a suspension of large particles in a density matched solvent truly duplicates both the radial and axial behavior of a pure liquid during the early stages of break off, images from the two situations should match up when appropriately synchronized to the same time $\bar{\tau}$. Fig. 5*B* demonstrates this explicitly by superimposing video images from pure water and a suspension of 0.7 mm diameter polyethylene particles in water. The boundaries from the pure fluid provide an excellent envelope for the average profile of the suspension.

The fact that force and length scales are intrinsically regularized by the finite particle size leads to two very remarkable features of this detachment. First, given that the forces involved are not divergent implies that the pressure expression derived here is generic and can be used to describe the stress at arbitrary suspension interfaces. A Laplace–Young type equation, modified to describe suspensions, could facilitate progress in constructing continuum descriptions for suspensions engaging in a variety of flows. For instance, a continuum description of boundary stresses could aid modeling technologies like inkjet printing (15, 41, 42), the fabrication of DNA microarrays (43), and omnidirectional

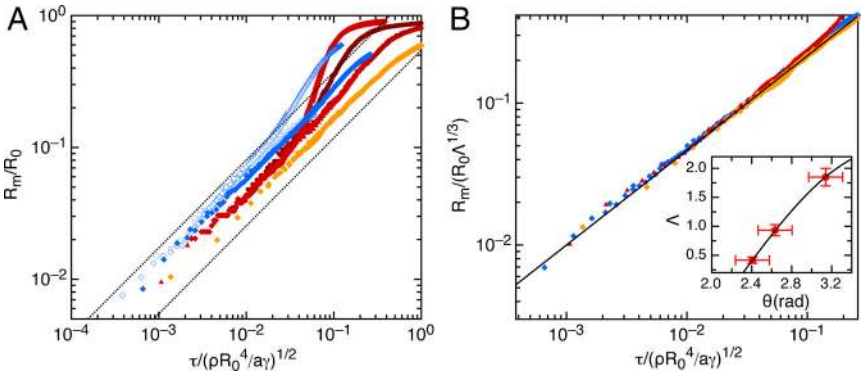

Fig. 4. (*A*) Dimensionless neck minimum radius as a function of dimensionless time. Data shown are 22 μm glass (blue diamonds) in water (solid) and oil (open) exiting a 4.7-mm nozzle, zirconium dioxide in water (red) with 150- and 250-μm particles exiting a 4.7-mm nozzle (triangles and light circles, respectively), as well as an 8.6-mm nozzle (diamonds and dark circles, respectively), and 200-μm polystyrene in water exiting a 4.7-mm nozzle (gold diamonds). The data collapses to within a prefactor of $\mathcal{O}(1)$. The remaining banding of the data demonstrates a material dependence of the power-law prefactor resulting from different particle-solvent combinations. (*B*) Forcing a collapse by to a single $\tau^{\frac{2}{3}}$ power law (see Eq. **2**) shows that the prefactor is directly related to the measured contact angle. (*Inset*) Dependence of the parameter Λ in Eq. **2** on liquid-particle contact angle θ.

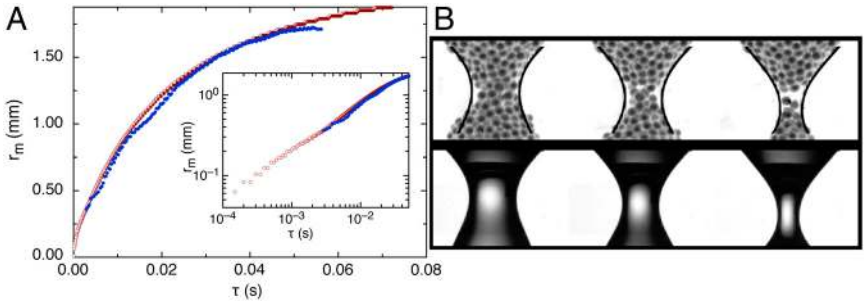

Fig. 5. (*A*) Neck radius r_{min} vs. time τ for water (red) and 0.7 mm ZrO_2 (blue) exiting from a 4.7-mm diameter nozzle. Because the nozzle size and particle size have become comparable, the suspension behaves just like the pure inviscid liquid and both thin together like $\tau^{\frac{2}{3}}$ (*Inset*). See Movie S4. (*B*) Sequence of snapshots for 0.71 mm polyethylene ($\rho = 1.0$ g/mL) in water (*Top*) and pure water (*Bottom*). Edges detected from the pure water images have been superimposed on the suspension images. With lengths rescaled by the initial nozzle diameter and videos appropriately synchronized, the fluid profile envelopes the suspension data because the scales describing particle driven pressure and Laplace–Young pressure are comparable.

printing (44), or more fundamental problems like the shear thickening in suspensions (32, 33) or jamming transitions in colloids mediated by capillary arrest (25).

Second, much like in bubble detachment (22–24), the system retains a memory of its initial conditions, specifically the initial nozzle radius, even though it undergoes a topological transition at detachment. Both systems are able to retain this memory through the help of an intrinsic length scale, which terminates the detachment before forces independent of the initial conditions diverge. In the case of bubbles this cutoff is provided by the asymmetry length scale (22) whereas for suspensions continuum modeling breaks down at the particle size. Moreover, the fact that the axial principal radius saturates implies that, also like bubble pinch-off, this type of detachment cannot be cast into a self-similar scaling class. Future work might examine the role of memory in this detachment process by imbedding asymmetries in the nozzle shape and analyzing the impact these have on the droplet profile.

Our findings show that droplet formation by suspensions bears similarities to pure liquid breakup but is not encapsulated by that theory. Particle deformations of the surface are not a perturbation that can be ignored through a limit case but rather provide a crucial ingredient to the force balance. A meaningful connection to pure liquids only exists far from the eventual singularity in the pure liquid, when the forces are comparable in scale to those of the suspension and the initial conditions are still relevant. Consequently, the system retains a memory of its initial conditions and fails to be self-similar even in the moments directly before breakup.

Materials and Methods

Our experiments employed two high-speed cameras synchronized to obtain a sufficiently large field of view together with high spatial resolution in the neck region (Fig. 1*B*). A Phantom v7.9 (Vision Research) was fitted with a Micro-Nikkor 55 mm 1:2.8 lens and Nikkon PK-12 ring extender to achieve a spatial resolution of 35 μm per pixel. A Phantom v7.3 was equipped with a bellows and macrolens giving 4.4 μm per pixel. Backlighting was provided by three Dedolight units (one for the camera imaging the large scale evolution, two for the bellows camera). This lighting allowed for shutter speeds around 100 μs for the large scale camera and 50 μs for the bellows camera.

Nondensity matched suspensions were prepared from soda lime glass (MoSci), zirconium dioxide (Glen Mills), and polystyrene particles (Grinding Media Depot) suspended in water or in different viscosity silicone oils (Clearco). For density matching, 1 g/mL polyethylene particles (Cospheric) were used in 20 cst silicone oil (Sigma Aldrich). The suspension was extruded from a variety nozzles at a constant rate by a syringe pump (Razel Scientific R99-E). Flow rates in the range of 10^{-4} mL/s kept the extrusion process quasi-static. To prevent fluctuations owing to variations in ambient conditions, the laboratory was controlled to stay at (50 ± 5)% humidity and at (72 ± 1) °F.

ACKNOWLEDGMENTS. We thank C. Bonnoit, E. Brown, J. Burton, E. Clement, J. Morris, and W. Zhang for insightful discussions. Additionally, we thank N. Keim for his image conversion software. This work was supported by the National Science Foundation (NSF) through CBET-0933242 and by the Keck Initiative for Ultrafast Imaging at the University of Chicago. The Chicago Materials Research Science and Engineering Center, supported by NSF under DMR-0820054, is gratefully acknowledged for access to its shared experimental facilities.

1. Eggers J (1997) Nonlinear dynamics and breakup of free-surface flows. *Rev Mod Phys* 69:865–930.
2. Eggers J, Villermaux E (2008) Physics of liquid jets. *Rep Prog Phys* 71:036601–036680.
3. Mosler M, Landman U (2000) Formation, stability, and breakup of nanojets. *Science* 289:1165–1169.
4. Kang W, Landman U (2007) Universality crossover of the pinch-off shape profiles of collapsing liquid nanobridges in vacuum and gaseous environments. *Phys Rev Lett* 98:064504.
5. Tiwari A, Reddy H, Mukhopadhyay S, Abraham J (2008) Simulations of liquid nanocylinder breakup with dissipative particle dynamics. *Phys Rev E Stat Nonlin Soft Matter Phys* 78:016305.
6. Aagesen LK, et al. (2010) Universality and self-similarity in pinch-off of rods by bulk diffusion. *Nat Phys* 6:796–800.
7. Lehner L, Pretorius F (2010) Black strings, low viscosity fluids, and violation of cosmic censorship. *Phys Rev Lett* 105:101102.
8. Gregory R, Laflame R (1994) The instability of charged black strings and p-branes. *Nucl Phys B* 428:399–434.
9. Zhang W, Robinson DN (2005) Balance of actively generated contractile and resistive forces controls cytokinesis dynamics. *Proc Natl Acad Sci USA* 102:7186–7191.
10. Lenz M, Morlot S, Roux A (2009) Mechanical requirements for membrane fission: Common facts from various examples. *FEBS Lett* 583:3839–3846.
11. Betterton MD, Brenner MP (2001) Collapsing bacterial cylinders. *Phys Rev E Stat Nonlin Soft Matter Phys* 64:061904.
12. Shi XD, Brenner MP, Nagel SR (1994) A cascade of structure in a drop falling from a faucet. *Science* 265:219–222.
13. van Hoeve W, et al. (2010) Breakup of diminutive Rayleigh jets. *Phys Fluids* 22:122003.
14. Thoroddsen ST, Etoh TG, Takehara K (2008) High-speed imaging of drops and bubbles. *Annu Rev Fluid Mech* 40:257–285.
15. Dong HM, Carr WW, Morris JF (2006) An experimental study of drop-on-demand drop formation. *Phys Fluids* 18:072102.
16. Burton JC, Rutledge JE, Taborek P (2004) Fluid pinch-off dynamics at nanometer length scales. *Phys Rev Lett* 92:244505.
17. Chen AU, Notz PK, Basaran OA (2002) Computational and experimental analysis of pinch-off and scaling. *Phys Rev Lett* 88:174501.
18. Chen Y, Steen P (1997) Dynamics of inviscid capillary breakup: collapse and pinchoff of a film bridge. *J Fluid Mech* 341:245–267.
19. Cohen I, Brenner MP, Eggers J, Nagel SR (1999) Two fluid snap-off problem: Experiment and theory. *Phys Rev Lett* 83:1147–1150.
20. Savage JR, Caggioni M, Spicer PT, Cohen I (2010) Partial universality: Pinch-off dynamics in fluids with smectic liquid crystalline order. *Soft Matter* 6:892–895.
21. Suryo R, Basaran O (2006) Local dynamics during pinch-off of liquid threads of power law fluids: Scaling analysis and self-similarity. *J Nonnewton Fluid Mech* 138:134–160.
22. Schmidt LE, Keim NC, Zhang WW, Nagel SR (2009) Memory-encoding vibrations in a disconnecting air bubble. *Nat Phys* 5:343–346.
23. Keim NC, Moller P, Zhang WW, Nagel SR (2006) Breakup of air bubbles in water: memory and breakdown of cylindrical symmetry. *Phys Rev Lett* 97:144503.
24. Doshi P, et al. (2003) Persistence of memory in drop breakup: The breakdown of universality. *Science* 302:1185–1188.
25. Cates M, Adhikari R, Stratford K (2005) Colloidal arrest by capillary forces. *J Phys Condens Matter* 17:S2771–S2778.
26. Binks BP, Horozov TS (2006) *Colloidal Particles at Liquid Interfaces* (Cambridge Univ Press, Cambridge, UK), pp 1–8.

27. Furbank R, Morris J (2007) Pendant drop thread dynamics of particle-laden liquids. *Int J Multiphase Flow* 33:448–468.
28. Hameed M, Morris J (2009) Breakup of a liquid jet containing solid particles: A singularity approach. *SIAM J Appl Math* 70:885–900.
29. Bonnoit C, Clément E (2010) Accelerated drop detachment in dense granular suspensions. arXiv:1009.1819 [cond-mat.soft].
30. Coussot P, Gallard F (2005) Gravity flow instability of viscoplastic materials: The ketchup drip. *Phys Rev E Stat Nonlin Soft Matter Phys* 72:031409.
31. Rutgers IR (1962) Relative viscosity of suspensions of rigid spheres in Newtonian liquids. *Rheol Acta* 2:305–348.
32. Brown E, et al. (2010) Generality of shear thickening in dense suspensions. *Nat Mater* 9:220–224.
33. Brown E, et al. (2010) The role of dilation and confining stress in shear thickening of dense suspensions. arXiv:1010.4921.
34. Royer JR, et al. (2009) High-speed tracking of rupture and clustering in freely falling granular streams. *Nature* 459:1110–1113.
35. Waitukaitis SR, Grütjen HF, Royer JR, Jaeger HM (2011) Droplet and cluster formation in freely falling granular streams. *Phys Rev E Stat Nonlin Soft Matter Phys* 83:051302.
36. Irvine WTM, Vitelli V, Chaikin PM (2010) Pleats in crystals on curved surfaces. *Nature* 468:947–951.
37. Nelson D (2002) *Defects and Geometry in Condensed Matter Physics* (Cambridge Univ Press, New York).
38. Modes CD, Kamien R (2008) Geometrical frustration in two dimensions: Idealizations and realizations of a hard-disk fluid in negative curvature. *Phys Rev E Stat Nonlin Soft Matter Phys* 77:071125.
39. Rubinstein M, Nelson D (1983) Dense-packed arrays on surfaces of constant negative curvature. *Phys Rev B* 28:6377–6386.
40. Gaspaard RM, Sadoc JF (1982) *The Structure of Non-Crystalline Materials*, eds PH Gaskell, JM Parker, and EA Davis (International Publications Service, New York).
41. Wijshoff H (2010) The dynamics of the piezo inkjet printhead operation. *Phys Rep* 491:77–177.
42. Li R, Ashgriz N, Chandra S (2008) Droplet generation from pulsed micro-jets. *Exp Therm Fluid Sci* 32:1679–1686.
43. Basaran O (2002) Small-scale free surface flows with breakup: drop formation and emerging applications. *AIChE J* 48:1842–1848.
44. Ahn BY, et al. (2009) Omnidirectional Printing of flexible, stretchable, and spanning silver microelectrodes. *Science* 323:1590–1593.

Supporting Information

Miskin and Jaeger 10.1073/pnas.1111060109

SI Text

Constant Axial Radius of Curvature. In a pure liquid, the axial length scale surrounding the minimum neck radius can become arbitrarily small, leading to universal structures which characterize the detachment process (Fig. 1*C*). Conversely, dense suspensions under detachment have a simpler structure: The axial curvature around the minimum stays fixed at a value set by the initial nozzle radius (Fig. S1). Here, we show both quantitative measurements of the axial curvature and present a basic model explaining how the axial curvature gets fixed as a consequence of constraints and volume conservation.

Near the neck minimum, the radius for a detaching suspension is approximately quadratic with the distance along the axis of symmetry z from the bridge minimum radius location which defines $z = 0$. By fitting a parabola to this region, we can extract a quantitative measure of the axial curvature scale at the neck minimum $z_m = \frac{\partial^2 r}{\partial z^2}$ (Fig. S2 *A*–*C*). Very early on, when the suspension has hardly been strained by gravity, this length scale is extremely large, owing the to cylindrical shape of the extruded plug. Then, when the strain from gravity becomes significant, the hanging plug develops a small indent on the profile, leading to a small axial length scale. This dent then widens as the drop detaches, increasing z_m. However, the widening gap quickly asymptotes to a fixed curvature. Plotting z_m with r_m against τ shows that the value of this asymptote is set by the initial nozzle radius and, as shown in Fig. S2*D*, plotting $\frac{z_m}{R_0}$ instead reduces all the asymptotes to $\frac{z_m}{R_0} \approx 1$.

To explain this fixed value, we consider the volume, V, which actually deforms during detachment. Measuring the initial length of the catastrophically deforming region suggests $V \approx \pi R_0^3$. Because this same region also makes up the subsequent bridge profile, then we also have $V = \int_{-l(\tau)}^{l(\tau)} \pi r(z)^2 dz = \int_{-l}^{l} \pi (r_m + \frac{1}{2}\frac{z^2}{z_m})^2 dz$ where the integrand comes from approximating the bridge profile as parabolic and $2l(\tau)$ is the length of the deformed region. We can estimate l by recognizing that any region outside the deformed zone must, by definition, have a radius equal to the initial nozzle's. Therefore, we can say $R_0 = r_m + \frac{1}{2}\frac{l^2}{z_m}$ or alternatively, $l = \sqrt{2 z_m (R_0 - r_m)}$. Evaluating the volume integral and setting it equal to the initial volume, we find that $\pi R_0^3 \sim 2\pi (r_m^2 l + \frac{r_m}{3 z_m} l^3 + \frac{1}{20 z_m^2} l^5)$. Finally, by substituting in the expression for l, and solving for z_m we find

$$z_m \sim \frac{225 R_0}{8(1 - \frac{r_m}{R_0})(3 + 4(\frac{r_m}{R_0}) + 8(\frac{r_m}{R_0})^2)^2}. \qquad \textbf{[S1]}$$

Taking the limit as $r_m / R_0 \to 0$ results in $z_m \to R_0$. That is, as the drop thins down, the axial curvature scale saturates around R_0.

Plotting Eq. **S1** with the data for r_m and z_m shows good qualitative agreement: There is an initial, cylindrical regime when the minimum radius is large, followed by a small dent regime with a local minimum in curvature and finally the drop enters the asymptotic regime. This agreement is quite good in spite of the simplicity of our model, asserting that the basic physical concepts governing the axial curvature scale are well represented. In particular, a model strictly using volume conservation and the fixed radius at the two symmetric boundaries is sufficient to lead to a fixed axial curvature scale approximately equal to R_0.

Granular Packings on Curved Surfaces. While there is an abundance of literature on locally ordered packings embedded in curved spaces, very little has been said about the disordered equivalent. Moreover, the model we developed to describe droplet detachment in dense suspensions features the hypothesis that particle arrangement on the surface of a 3D packing couples to Gaussian curvature. Specifically, we argue that in regions of high curvature, both the surface area per particle S_{pp} and the mean coordination number $\tilde{Z}$ are altered by the Gaussian curvature, K. To strengthen this hypothesis, we perform simulations of granular sphere packings, and by both triangulating the particles and computing the surface area per particle, we find that ensemble averages of these values do depend on the Gaussian curvature in a simple way.

To keep a strong correspondence between the simulations and the experiments, the surfaces we use for packing are extracted directly from the experiment. We find that, to a good approximation, the dimpled bridge profile describing a detaching drop can be enveloped by a hyperboloid of one sheet (Fig. S3 *A* and *C*). To emulate the detaching drop, we randomly fill a large cylindrical space with spheres until the excluded volume prohibits the addition of spheres. Next, we remove all the spheres with centers outside of a bounding hyperboloid, which is slightly bigger than the bridge profile. To emulate the surface tension, we add elastic walls on along the boundary of the hyperboloid and allow them to press in the spheres along the edge. Because the packings are supposed to relate to configurations that exist for fractions of a second, we press the spheres in while reseting the velocities every few cycles. Doing so prevents spheres from artificially escaping into the bulk, and ensures that the surface area associated with each particle is equilibrated only through collisions.

For analysis, we construct a contracted boundary by shrinking the radius of the hyperboloid by some amount, δ. Specifically, δ is chosen so that, when the hyperboloid used to construct the packing is contracted inward by δ, the angle connecting the top of a protruding sphere to the surface matches the experimentally estimated value of 50°. Moreover, shifting the radius by a constant also ensures that, like in the experiment, the axial radius of curvature is left invariant during the contraction. One minor complication that arrises from this boundary definition is that the Gaussian curvature deviates from that of an exact hyperboloid. Instead, if the hyperboloid used for the packing is defined by $\frac{r^2}{r_m} - \frac{z^2}{z_m^2} = 1$, then the shape defined by $r \to r - \delta$ will have a curvature $K = \frac{z_m^2 \sqrt{z^2 + z_m^2}}{(\delta(\frac{z_m}{r_m}) - \sqrt{z^2 + z_m^2})(z^2(1 + (\frac{r_m}{z_m})^2) + z_m^2)^2}$. In this form, the expression for a real hyperboloid's Gaussian curvature is recovered if $\delta \to 0$.

Fig. S3 *A* and *B* and *D* and *E* show side by side comparisons of the experimental data and the simulation used to emulate it. The images illustrate the strong qualitative similarities between the profiles, and the shapes and distributions of particle deformations.

By constructing two types of simulations, one describing the early stages of scaling and the other late in detachment, we can explicitly examine the packing structure for the surface of interest. Conformally mapping the points on the surface to a disk and performing a Delaunay triangulation gives us the coordination numbers for each particle (Fig. S3 *C* and *F*). Moreover, by binning positions along the axis of symmetry, we can define S_{pp} for a given height along the hyperboloid. Bins are chosen to be one particle radius apart from each other. To avoid unphysical boundary effects, we throw out the first three bins from the

boundary. If our model is correct, then both of these parameters should be impacted by the curvature.

After ensemble averaging 1,000 simulations we find strong evidence that both the coordination number and surface area per particle depend on the Gaussian curvature (Figs. S4 and S5), particularly for profiles associated with scaling. In this regime, K is an excellent replacement for $\frac{\bar{Z}}{S_{pp}}$ across the surface (Fig. S4). Further the surface area per particle and coordination number both clearly relate to the curvature of the shape (with $\bar{Z} \approx 6.3$). Conversely, just before the onset of scaling when the curvature is smaller, these features are qualitatively similar, albeit less pronounced. At this point in time, $\bar{Z}$ is lower at 6.1 and features in S_{pp} are less obvious. However, we still find that K is still an excellent replacement for $\frac{\pi}{3}(6-\bar{Z})/S_{pp}$ (Fig. S5).

These simulations also allow us to calculate exactly how $\bar{Z}$ depends on K. The simplest guess is that the spheres simply pack as tightly as possible on the surface. This would require that the coordination number for each particle is given by the number of spheres that can be packed in contact around a central sphere, or $2\pi/\arccos\frac{\cosh 2\sqrt{-Ka}}{1+\cosh 2\sqrt{-Ka}}$. In the limit that $\sqrt{-Ka}$ is small, this expression can be expanded out to second order in $\sqrt{-Ka}$ as $\bar{Z} \approx 6 - \frac{6\sqrt{3}}{\pi} Ka^2$. Plotting values for Ka^2 from the simulations against $\bar{Z}$ shows good agreement with the linear behavior, but the slope of the line is a factor of two too large (Fig. S6*A*). We interpret this result by noting the 3D nature of the packing. When the spheres are pressed in by the elastic walls, particles in the bulk can mediate an interaction between particles actually on the surface. This can create an the effective radius that can be anywhere between one to two times the actual particle radius (Fig. S6*B*). Our measured increase would suggest the physically acceptable effective radius of $\sim\sqrt{2}a$.

Altogether these results provide strong support for the equations used in deriving our scaling relations: they confirm that both early and late in the scaling regime, $K = \frac{\pi}{3}(6-\bar{Z})/S_{pp}$ and show that $\bar{Z}$ is set simply by the densest packing of circles, with an effective radius created by particles interacting through the bulk. Moreover, the strength of this agreement suggests that these results may be generic statements about granular sphere packings, independent of the assembly process; however, further investigation is needed to be certain.

Derivation of the Scaling Relation. Starting with the simple pressure expression derived in the text and the Navier–Stokes equations, we derive a scaling relation for $r_m(\tau)$.

We start by identifying the characteristic axial and radial length scales associated with the flow. Because the pressure is all localized around the neck minimum radius, the natural choice for the radial length scale is r_m. To find the characteristic z length scale, we note that the axial radius of curvature is a fixed value, R_0. Because the axial radius of curvature near the neck minimum is defined by $1/R_0 = \frac{\partial^2 R}{\partial z^2}$, we can identify the characteristic length for z as $\sqrt{R_0 r_m}$.

To simplify the full Navier–Stokes equations we make some assumptions about the flow from both symmetry and the granular nature of the suspension. First, because the shape of the detaching drop is cylindrically symmetric, we assume that all gradients in the ϕ direction as well as v_ϕ vanish. This implies that any vorticity to the flow $(\nabla \times \vec{v})$ is given by one component:$\nabla \times \vec{v} = \hat{\phi}(\frac{\partial v_r}{\partial z} - \frac{\partial v_z}{\partial r})$. In order for this quantity to be large, there must be a large rotation associated with velocities as viewed in the r, z plane. However, if this were to happen, flow would eventually need to push into either the bounding fluid or the jammed bulk outside of the neck minimum area. For either case to occur, there would need to be a pressure from the bulk larger than the confining stress. Because any pressure in the bulk is created by force chain propagation from the boundary, this cannot not happen. Additionally, the presence of a large rotational flow would require some sort of a pressure gradient along the r direction. Again, the presence of force chains will suppress any radial pressure gradients. Altogether, these observations suggest that to a good approximation $\frac{\partial v_r}{\partial z} - \frac{\partial v_z}{\partial r} \sim 0$. In other words, we assume the flow is irrotational.

Using these results, we can greatly simplify the Navier–Stokes equations:

$$\rho\left[\frac{d\vec{u}}{dt} + \vec{u}\cdot\nabla\vec{u}\right] = -\nabla P + \mu\nabla^2\vec{u} \qquad \textbf{[S2]}$$

$$\nabla\cdot\vec{u} = 0. \qquad \textbf{[S3]}$$

If we rewrite the vector Laplacian and exploit the volume conservation Eq. 3, we have

$$\rho\left[\frac{d\vec{u}}{dt} + \vec{u}\cdot\nabla\vec{u}\right] = -\nabla P - \mu\nabla\times(\nabla\times\vec{u}). \qquad \textbf{[S4]}$$

The last term must vanish if the flow is irrotational, reducing to inviscid flow. We note, again, that the experimental results are independent of solvent viscosity during the detachment, thereby supporting the assumption of irrotational flow. The Navier–Stokes equations now can be written as the Euler equations for this flow:

$$\rho\left[\frac{d\vec{u}}{dt} + \vec{u}\cdot\nabla\vec{u}\right] = -\nabla P. \qquad \textbf{[S5]}$$

Inserting the characteristic length and time scales gives the scaling relation for u_z.

$$\rho\frac{u_z}{\tau} \sim \frac{P}{\sqrt{R_0 r_m}} \qquad \textbf{[S6]}$$

Using the irrotational flow assumption, $\frac{\partial v_r}{\partial z} = \frac{\partial v_z}{\partial r}$, we can argue that $\frac{v_r}{\sqrt{r_m R_0}} \sim \frac{v_z}{r_m}$. We can now rewrite the scaling relation in terms of the measured variable, r_m.

$$\rho\frac{u_r}{\tau} \sim \frac{P}{r_m} \qquad \textbf{[S7]}$$

$$\rho\frac{r_m}{\tau^2} \sim \frac{P}{r_m} \qquad \textbf{[S8]}$$

Inserting the pressure expression derived in the main text gives the scaling relation which collapses our data:

$$r_m \sim \left(\frac{\Lambda\gamma a}{\rho R_0}\right)^{\frac{1}{3}}\tau^{\frac{2}{3}}. \qquad \textbf{[S9]}$$

Rheological Characterization. In this section we review some basic features of dense suspension rheology and present data collected from both parallel plate and Couette cell geometry rheometers. We find, in agreement with the literature, that the zero shear limit viscosity of dense suspensions diverges near jamming. More generally, we find that for dilute suspensions, a single viscosity value can adequately describe the behavior of the bulk, whereas shear stress typically depends on shear rate nonlinearly when the suspension is dense. Finally we interpret these results in the context of present fluid pinch of literature. We conclude that the detachment models presently available in the literature cannot characterize dense suspension snap-off.

Fig. S7 plots viscosity against shear rate for suspensions made from 33 um polyethylene in a 20 cst solvent oil of the same density (1.01 g/mL). The data were acquired using a Couette cell geometry. Each curve is at a different packing fraction and a measurement consists of a sweep from low shear rate to high and then back to low to ensure the system was in a steady state. We note that the basic effect of the particles is to increase the magnitude of the solvent viscosity. Indeed, plotting the magnitudes of viscosity against the packing fraction shows that the data can be well fit by a Krieger–Dougherty model (S1), $\mu = \mu_0(1 - \phi/\phi_j)^{-n}$ where μ_0 is the solvent viscosity, ϕ_j is the jamming packing fraction and n is some $\mathcal{O}(1)$ exponent. Our data is well fit with the correct solvent viscosity (fit viscosity was 19.7 cst), $\phi_j = 0.57$ and $n = 1.62$.

Up to $\phi = 0.5$, the viscosity of the suspension is essentially independent of shear rate. That said, one might attempt to characterize the breakup, as is standard in pinch-off literature, using the Ohnesorge number, $Oh = \mu/\sqrt{l\gamma\rho}$ where l is the characteristic length scale of the problem. This dimensionless number compares the relative importance of viscous dissipation to inertia and surface tension.

We think that this approach is of little value for suspensions. First consider a $\phi = 0.5$, $\mu_{\text{eff}} = 1{,}000$ cSt suspension detaching from a 2.35 mm radius nozzle (Fig. S8). Suppose the relevant length scale is r_m. Because $r_m \leq R_0$ we have $Oh \geq 2$. This characterization states the viscosity is always at least as relevant as surface tension and inertia, yet the observed $2/3$ scaling demonstrates the opposite. In fact, because a pure oil with a viscosity of 50 cSt will exhibit linear scaling near detachment (Fig. 3*C*), the Oh estimate would predict that, given all other parameters are fixed, any suspension with a packing fraction above $\phi = 0.25$ should display linear scaling near breakup. This is again incompatible with the data: The suspensions with $\phi = 0.25$ (see Fig. 3*C*) and denser (S2) all show a regime compatible with $2/3$ scaling. Altogether these results suggest that the standard Ohnesorge number does not appropriately characterize the breakup of suspensions, even in the dilute limit.

Now consider packings closer to jamming. For dense suspensions, the viscosity fails to be a single material parameter and instead begins to depend sensitively on packing fraction and shear rate (S3). While the scale of the viscosity can jump over an order of magnitude depending on a single percent of packing fraction, the typical lower bound estimate for the viscosity is still tremendously large. For instance at a shear rate of 100/s, a suspension at $\phi = 0.55$ made of 100 μm glass in water has a viscosity, surface tension and density all within about 40% of glycerol (S4). To us, this makes it all the more surprising that the snap-off of this suspension is characterized by $2/3$ scaling.

One could argue that it would be more relevant to consider a local estimate for Oh and use the particle size as the relevant length rather than r_m. Again the data suggests against this. Consider the two oil based suspensions in Fig. 3*A*. Using the particle size (22 μm), solvent viscosity (100 cP/1 cP), surface tension (20 mN/m) and the density (1.8 g/cm^3), the Ohnesorge number is 3.5 for the 100 cP solvent and 0.035 for the 1 cP solvent. The fact that the curves fall on top of each other for the regime directly before snap-off suggest this local measure for the Oh does not capture the relevant physics.

Moreover, we could push all of these arguments further by noting that the flowing suspension should not have a viscosity lower than that of the solvent. Thus, if the solvent alone were outside the inviscid regime, then the suspension should not behave inviscidly. The suspension of glass particles in 100 cP oil shows this reasoning is again incorrect: while a 100 cP oil will detach as a viscous liquid, a suspension's behavior is much more similar to the inviscid case.

Finally we consider the possibility that the detachment is characterized by models developed for generic power-law fluids. In these models (S5, S6) the neck minimum radius thins with the same exponent, which relates the shear rate to the shear stress. For suspensions, this approach is troubled on a few counts. First, the exact nature of the shear exponent is highly dependent on packing fraction (S3). As the drop detaches, it forms more surface area. As particles emerge from the bulk and protrude through this area, the internal packing fraction must drop. That said, the idea of associating a single $2/3$ exponent when the shear rheology exponent can change dramatically seems questionable. Second, the same $2/3$ exponent holds into the dilute limit, where the suspensions are effectively Newtonian, from a rheological point of view. If the $2/3$ exponent had emerged from power-law fluid behavior, then it should change when the suspension becomes sufficiently dilute. Last, the bridge profile is predicted to be self-similar for power-law fluid models, whereas the profile for suspension pinch off is not.

To our knowledge, these approaches summarize the extent of quantitatively predictive models rooted in rheological measurements, which are potential candidates for describing suspension pinch off. Evidently each of them is lacking in some respect. Estimates comparing the viscous to inertial and surface tension scales developed for pure liquids do not seem to relate to the detaching suspension, regardless of whether they are used on the global or local scale. Moreover, models developed for power laws are questionable as well because the shear rate to shear stress exponent in dense suspensions is highly sensitive to packing fraction and the same exponent persists when shear stress becomes proportional to shear rate.

We speculate that the inadequacy of these models is related to the fact that the boundary conditions that confine a suspension are essential in dictating its shear response. The free surface boundary associated with pinch off is fundamentally different from the boundary conditions of any standard shear rheometer: in snap-off the geometry and internal stress control each other. This difference in boundary condition may also lead to a difference in shear stress response, which causes these approaches to fall short.

1. Rutgers IR (1962) Relative viscosity of suspensions of rigid spheres in Newtonian liquids. *Rheol Acta* 2:305–348.
2. Bonnoit C, Clément E (2010) Accelerated drop detachment in dense granular suspensions. arXiv:1009.1819 [cond-mat.soft].
3. Brown E, et al. (2010) Generality of shear thickening in dense suspensions. *Nat Mater* 9:220–224.
4. Binks BP, Horozov TS (2006) *Colloidal Particles at Liquid Interfaces* (Cambridge Univ Press, Cambridge, UK).
5. Savage JR, Caggioni M, Spicer PT (2010) Partial universality: Pinch-off dynamics in fluids with smectic liquid crystalline order. *Soft Matter* 6:892–895.
6. Suryo R, Basaran O (2006) Local dynamics during pinch-off of liquid threads of power law fluids: Scaling analysis and self-similarity. *J Nonnewton Fluid Mech* 138:134–160.

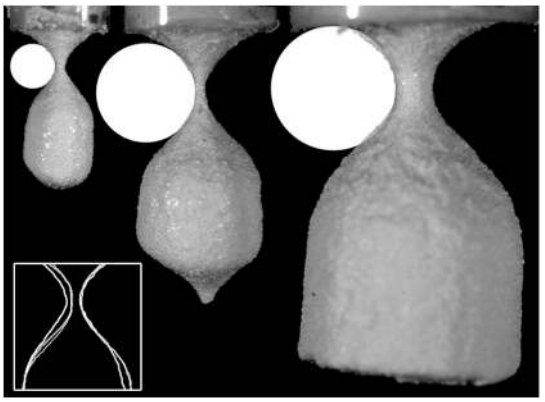

Fig. S1. Images for dense suspensions of 250 μm zirconium dioxide particles suspend in water exiting a 4.7 (*Left*), 8.6 (*Center*), and 14.5 (*Right*) mm diameter nozzles. Circles representing the axial radii of curvature have been drawn on top, making it clear that the radius of each circle is comparable to the radius of the nozzle. Moreover, if the images are scaled by their respective initial radii, then superimposing the edges from all three leads to an overlap of the roughly parabolic structure (see *Inset*).

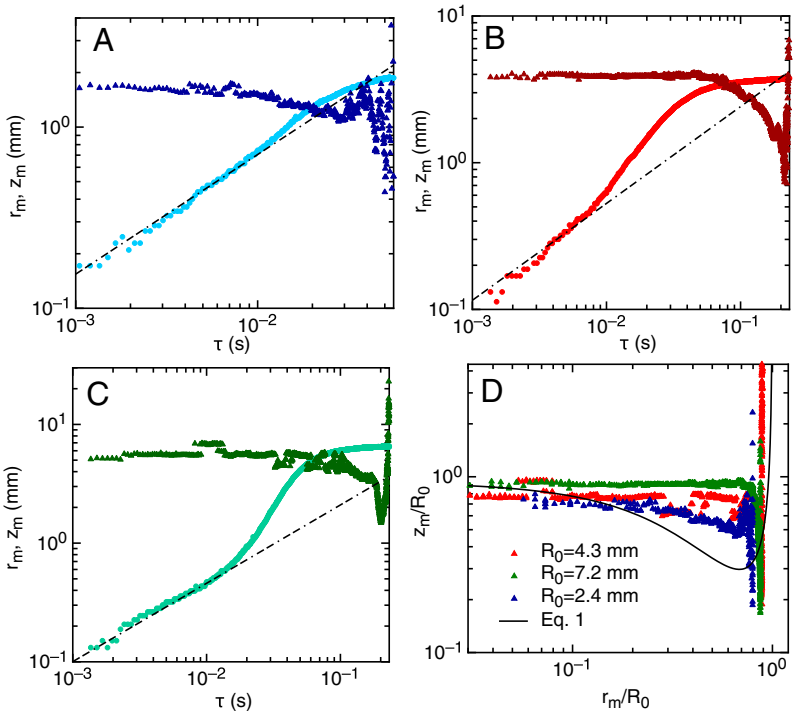

Fig. S2. (*A*–*C*) r_m (light symbols) and z_m (dark symbols) for dense suspensions of 250 μm zirconium dioxide particles suspend in water exiting 4.7 mm (*A*), 8.6 mm (*B*), and 14.5 mm (*C*) diameter nozzles. Initially, the drop has an infinitely large axial radius of curvature z_m, due to the undeformed, cylindrical shape. This radius decreases as the drop begins to detach, hits a minimum, and then increases asymptotically to a value set by the initial nozzle radius. (*D*) Plotting the dimensionless principle radii, r_m/R_0 and z_m/R_0, collapses the data to the same order of magnitude and shows good qualitative agreement with the model represented by Eq. **S1**.

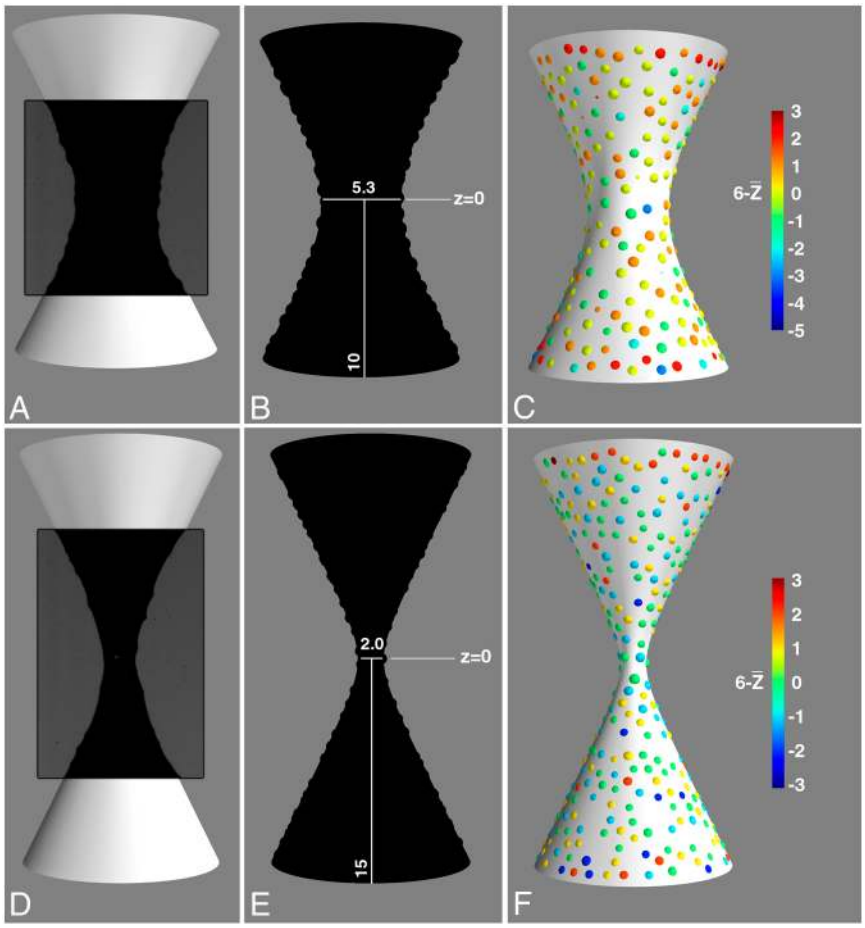

Fig. S3. (*A* and *D*) Photographs taken from our experiment showing the bridge profile at the onset of scaling (*A*) and deep in the scaling regime (*D*). Drawn in white are the hyperboloids used as walls in generating our simulated packings. (*B* and *E*) Data from the simulations in both regimes rendered to be backlit. Comparing the simulated results in the center to the experimental data on the left shows that the bridge profile is well represented as is the general density and size of deformations. The dimensions of the hyperboloid have been drawn in for reference with lengths nondimensionalized by the particle diameter (145 μm). (*C* and *F*) The same simulation data with coloring based on coordination number.

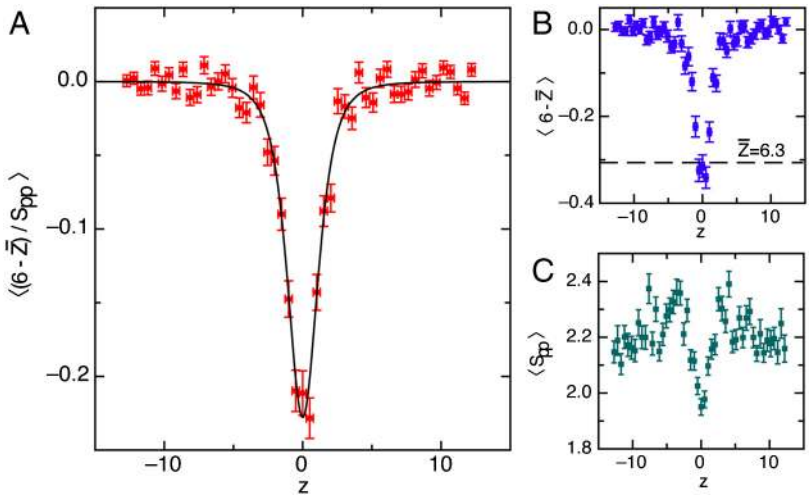

Fig. S4. Ensemble average of $(6-\bar{Z})/S_{pp}$ (*A*), $\bar{Z}$ (*B*), and S_{pp} (*C*) associated with a bridge profile deep into the scaling regime. The *z* axis corresponds to the axis of symmetry and $r(z=0)=r_m$. Deep in the scaling regime $\bar{Z}$, S_{pp}, and $\frac{6-\bar{Z}}{S_{pp}}$ are all clearly related to the curvature. There is excellent agreement between $\frac{6-\bar{Z}}{S_{pp}}$ and $\frac{3}{\pi}K$, as required by our model (*A*). Further $\bar{Z}$ is set by the curvature (*B*): curved regions feature more nearest neighbors while regions with no curvature have six nearest neighbors. Finally, we note that S_{pp} starts to increase in the regions with curvature but then quickly decreases at the neck minimum (*C*). We attribute this minimum to finite size effects since for this simulation the neck is merely two diameters across.

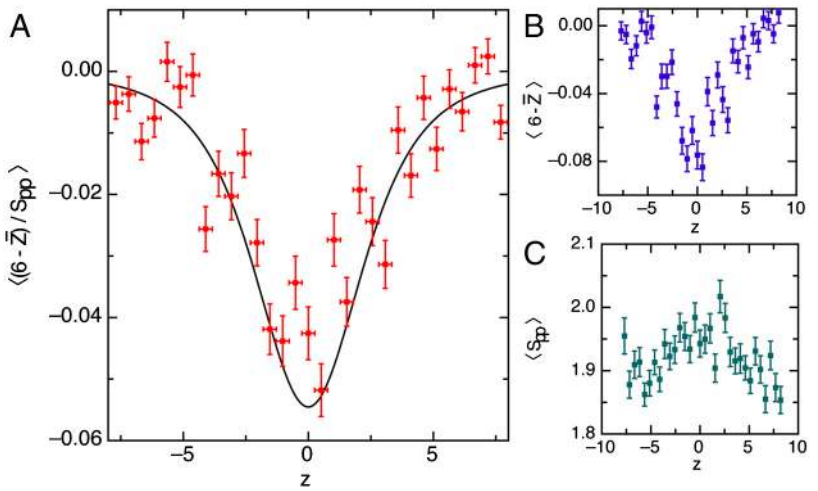

Fig. S5. Ensemble average of $(6-\bar{Z})/S_{pp}$ (*A*), $\bar{Z}$ (*B*) and S_{pp} (*C*) for a bridge profile at the onset of scaling. Values measured for $(6-\bar{Z})/S_{pp}$ still show good agreement with $\frac{3}{\pi}K$ (black line) (*A*) and there remain more nearest neighbors on average in the regions of high curvature (*B*). The surface area per particle appears to slightly increase around the neck minimum, as anticipated by our model (*C*). The relatively shallow slope presumably relates to the fact that this data is for the onset of scaling, where curvature effects are just beginning to be relevant.

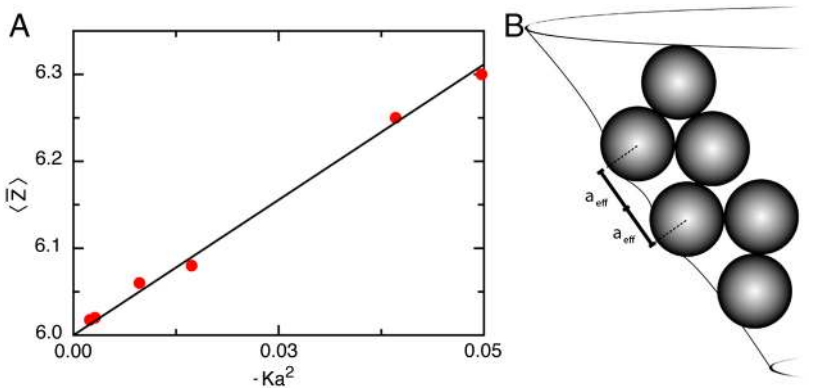

Fig. S6. (*A*) Ensemble average of the coordination number as a function of curvature and sphere radius. Note the largest four points correspond to values from the simulation data in Figs. S4 and S5 whereas the lowest two were obtained from additional simulations performed on the highly curved hyperboloid (Fig. S3 *E–F*) with smaller spheres ($a_{small} = 0.2a_{large}$). The linear trend displayed by the data is anticipated for the densest packings of circles on a curved space; however, the slope of the line is larger than anticipated. This is due to the 3D nature of the packing, which can mediate particle interactions creating an effective radius. (*B*) An illustration of how particles interacting through the bulk can be given an increased effective radius.

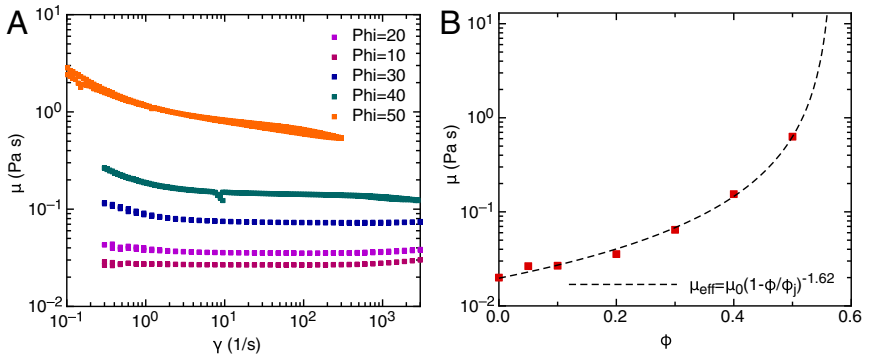

Fig. S7. (*A*) Viscosity vs. shear rate for suspensions with packing fractions from 0.1 to 0.5. The suspensions are made from 33 μm polyethylene in a density matched 20 cSt oil. In this regime, the viscosity is sufficiently constant over a range of shear rates and monotonically increases with packing fraction. (*B*) Effective viscosity of suspension against the packing fraction. The viscosities are well fit by a Krieger–Dougherty model with a jamming packing fraction of 0.57 and an exponent of 1.62.

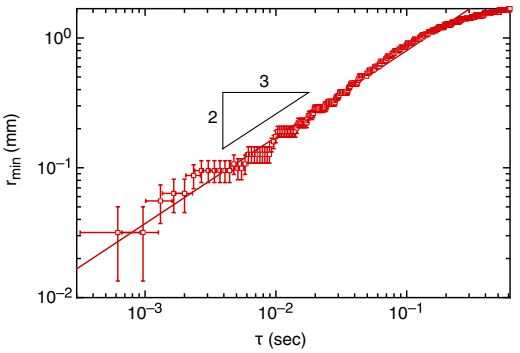

Fig. S8. r_{min} vs. τ for a $\phi = 0.5$ suspension of 33 μm polyethylene in 20 cSt silicone oil. The effective viscosity of the suspension should be near 1,000 cSt, yet the breakup is much more compatible with 2/3 scaling than with linear scaling. Note that for the $\phi = 0.5$ suspension, it was too difficult to predict where the final pinch off will take place, and so using the two camera setup was not possible. This limited our resolution to that of a single camera. This decreased our temporal resolution, and to compensate we averaged over points.

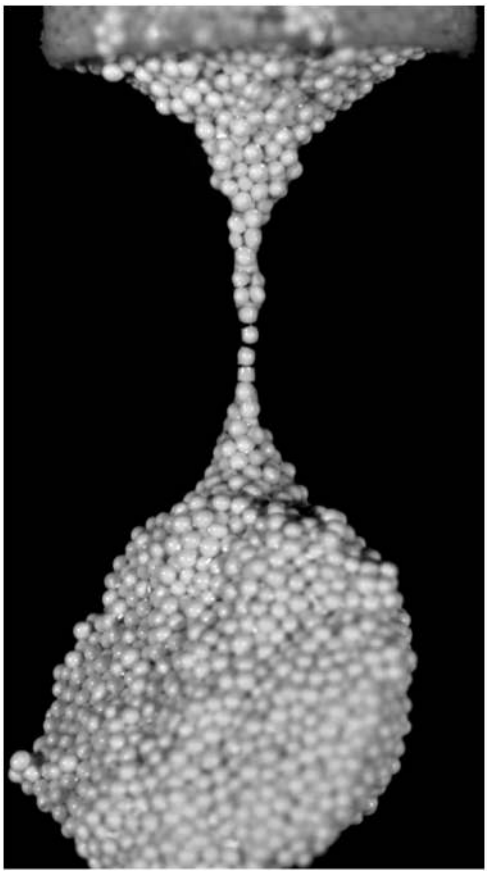

Movie S1. Front light movie of a suspension droplet made from 850 μm zirconium dioxide suspended in water detaching from a 14.5 mm diameter nozzle. The symmetric profile maintains itself until the neck is only one particle thick, and the small liquid bridge adjoining particles ruptures. The remaining tendril then forms a small satellite drop.

Movie S1 (MOV)

Movie S2. Back light movie combining data from our two camera setup of pure 50 cst silicone oil detaching from a 4.7 mm diameter nozzle. The profile of the drop starts symmetric, but as thinning continues turns over into an asymmetric self-similar scaling profile. Note that the neck minimum radius data corresponding to this movie may be found in Fig. 3*C*.

Movie S2 (MOV)

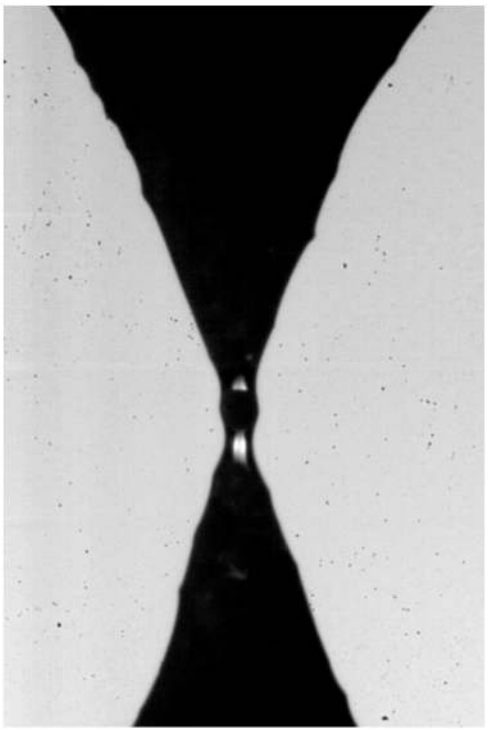

Movie S3. Back light movie combining data from our two camera setup of 145 μm zirconium dioxide particles suspended in water detaching from a 4.7 mm diameter nozzle. Unlike the viscous pinch off, the profile of the detaching drop remains symmetric right up to the final moment of rupture.

Movie S3 (MOV)

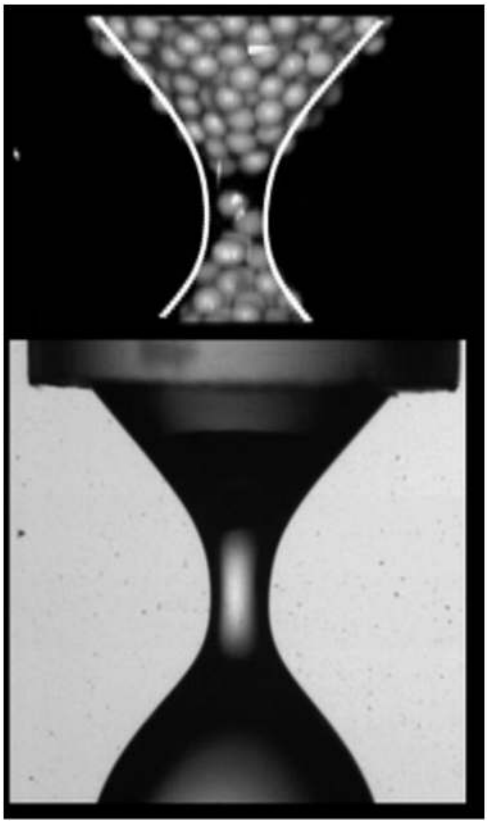

Movie S4. Movie juxtaposing 0.71 mm polyethylene ($\rho = 1.0$ g/mL) in water (*Top*) and pure water (*Bottom*). Edges detected from the pure water images have been superimposed on the suspension images. With lengths rescaled by the initial nozzle diameter and videos appropriately synchronized, the fluid profile envelopes the suspension data because the scales describing particle driven pressure and Laplace–Young pressure are comparable.

Movie S4 (MOV)